






Real-space thermalization of locally driven quantum magnets

Ronald Melendrez ^{1,2}, Bhaskar Mukherjee ³, Prakash Sharma ^{1,2}, Arijeet Pal ³, and Hitesh J. Changlani ^{1,2}

¹*Department of Physics, Florida State University, Tallahassee, Florida 32306, USA*

²*National High Magnetic Field Laboratory, Tallahassee, Florida 32310, USA*

³*Department of Physics and Astronomy, University College London, London WC1E 6BT, United Kingdom*

 (Received 16 March 2024; revised 2 August 2024; accepted 2 August 2024; published 9 September 2024)

The study of thermalization and its breakdown in isolated systems has led to a deeper understanding of nonequilibrium quantum states and their dependence on initial conditions. The role of initial conditions is prominently highlighted by the existence of quantum many-body scars, special athermal states with an underlying effective superspin structure, embedded in an otherwise chaotic many-body spectrum. Spin Heisenberg and XXZ models and their variants in one and higher dimension have been shown to host exact quantum many-body scars, exhibiting perfect revivals of spin helix states that are realizable in synthetic and condensed matter systems. Motivated by these advances, we propose experimentally accessible, local, time-dependent protocols to explore the spatial thermalization profile and highlight how different parts of the system thermalize and affect the fate of the superspin. We identify distinct parametric regimes for the ferromagnetic (X -polarized) initial state based on the interplay between the driven spin and the rest, including local athermal behavior where the driven spin effectively decouples, acting like a “cold” spot while being instrumental in heating up the other spins. We also identify parameter regimes where the superspin remains resilient to local driving for long timescales. We develop a real- and Floquet-space picture that explains our numerical observations, and make predictions that can be tested in various experimental setups.

DOI: [10.1103/PhysRevB.110.104304](https://doi.org/10.1103/PhysRevB.110.104304)

I. INTRODUCTION

In a set of pioneering papers [1–4] the question of thermalization of isolated quantum systems was posed sharply and addressed. It is now understood that generic isolated quantum systems satisfy the eigenstate thermalization hypothesis [5]. Broadly said, local observables are insensitive to the choice of eigenstate at a given energy density and the system is “self-thermal,” i.e., it acts as its own heat bath. However, there are important exceptions, these include emergent integrable systems, for example, many-body localized systems [6–10], and partially integrable systems or those with “quantum scars” [11–14]. The search for quantum many-body scars (QMBS), athermal states embedded in the spectra of otherwise chaotic systems, has seen recent activity [13–36] because of fundamental interest and due to proposals for using them for quantum sensing [35,37]. Though not expected for generic interacting systems [38], QMBS states do occur in realistic situations, especially when the Hilbert space is fragmented due to kinetic constraints [24,39–42]. In a time-dependent setting, the presence of a global periodic drive can either destabilize or stabilize prethermal/athermal behavior associated with QMBS [43–45], for example, under certain conditions the system can exhibit slow thermalization and dynamical freezing [46,47].

In previous work, some of us identified the XXZ model as a simple platform for realizing QMBS and Hilbert-space fragmentation (HSF) [23,24]. The model shares a common unifying theme with other models of scars, including the widely studied PXP one [14]; there is a “superspin” whose precession is responsible for revivals in various numerically computed and experimentally measured physical observables.

Such a superspin can be realized as a ferromagnetic state embedded in the middle of the many-body energy spectrum [the exact $SU(2)$ degeneracy being split by a magnetic field] by “staggering” the XXZ model, i.e., by alternating the sign of interactions on different geometric motifs [23]. In one dimension this translates to a Hamiltonian with alternating nearest-neighbor ferromagnetic and antiferromagnetic interactions. When the spins are prepared in a collective coherent state, for example in the $|X\rangle \equiv \prod_i \otimes |\rightarrow\rangle_i$ state, and allowed to time evolve, their dynamics corresponds to that of a superspin. The interactions between the spins are rendered completely ineffective by the choice of initial conditions and there is no thermalization [23]. However, this is a fine-tuned situation and one should generically expect thermalization when the system is perturbed.

The question we ask here is as follows: How do QMBS thermalize when subjected to time-dependent fields? Our motivation stems from the aim of expanding the existing dichotomy of classifying a system as either thermal or athermal. After all, could it be that there are parts of the system that are athermal (or prethermal on long timescales) while the rest have thermalized? We explore this question in the context of a periodic, local drive [48–50], and demonstrate the crossover between regimes of weak HSF and quantum scarring where the system locally remains athermal (on the timescale of the observation) due to the interplay between the dynamics of the driven spin and the rest of the system. We investigate two time-dependent potentials, schematically depicted in Figs. 1(a) and 1(b) whose similarities and differences we will highlight, especially in the context of the effective Floquet Hamiltonian they realize. In both cases the Hamiltonian for a N site spin-1/2 chain is given by $H = H_0 + H_D(t)$,

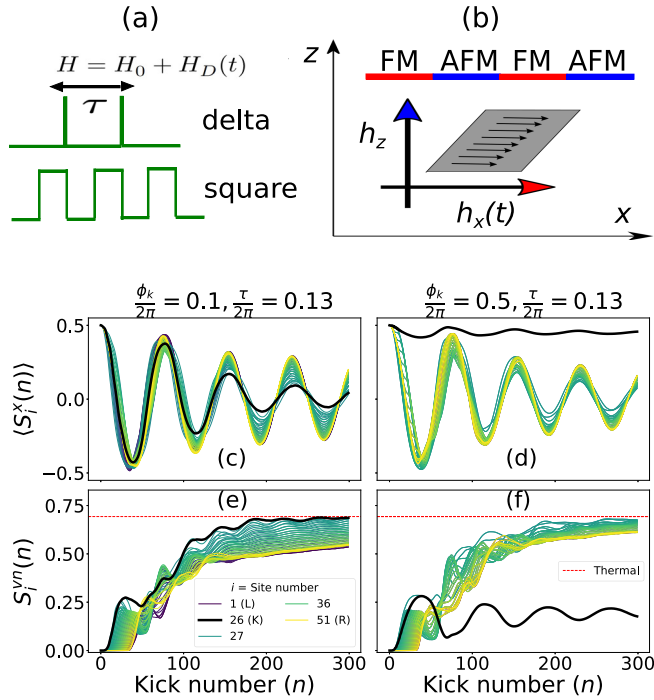


FIG. 1. Schematic of (a) local kick protocols and (b) the system studied in this work. The alternating (staggered) interactions place the ferromagnetic state in the middle of the spectrum. For the local delta kick, we show two characteristic behaviors for a $N = 51$ site system with open boundary conditions with the kick at the central site (labelled by K). Panels (c) and (d) show $\langle S_i^x \rangle$ and (e) and (f) the von Neumann entanglement entropy of representative sites. Results are for $J = 1$, $h = 0.1$, $\tau/2\pi = 0.13$ and [(c) and (e)] $\phi_k/2\pi = 0.1$ and [(d) and (f)] $\phi_k/2\pi = 0.5$. The driven site thermalizes for weak kicks, for stronger kicks, it remains athermal on the timescale of observation. The numerical simulations were performed with TEBD, as discussed in the text. Labels L and R refer to the leftmost and rightmost edges of the chain respectively.

where

$$H_0 \equiv J \sum_{i=1}^N (-1)^i \mathbf{S}_i \cdot \mathbf{S}_{i+1} - h \sum_{i=1}^N S_i^z \quad (1)$$

and $H_D(t)$ is a time-dependent drive term. $\mathbf{S}_i \equiv (S_i^x, S_i^y, S_i^z)$ refer to the usual spin-1/2 operators on site i , J (set to 1 throughout) is the alternating (staggered) ferro- and antiferromagnetic interaction strength and h is the strength of the magnetic (Zeeman) field. $i + 1$ is taken modulo N for periodic boundary conditions. For open boundary conditions the index i on the first sum runs from 1 to $N - 1$. Unlike the (Bethe ansatz) integrable uniform Heisenberg chain [51], H_0 is known to be nonintegrable [52]. Its study, primarily in the context of its ground-state properties, has a long history due to its relevance to Haldane spin chains [53–55].

For the first “delta kick” protocol, the drive term is

$$H_D(t) \equiv - \sum_{n>0} \sum_i \phi_i S_i^x \delta(t - n\tau), \quad (2)$$

where ϕ_i denotes the strength of the applied transverse (direction taken to be x) magnetic field strength on site i . The

delta kick can be thought of as a reasonable approximation to the situation where the duration of the transverse field pulse is much shorter than τ and other timescales associated with H_0 (e.g., $1/J$ and $1/h$). While there is a considerable body of work on models where a single large spin is kicked [56–58], we emphasize that H_0 here has only local interactions and the system behaves as a collective spin (superspin) degree of freedom only for certain initial conditions. We consider the case where only a single spin at site k is driven with strength ϕ_k , while the rest of the spins are undriven.

The second drive protocol is that of a symmetric square pulse,

$$H_D(t) \equiv \sum_i \gamma_i \text{Sgn} \left(\sin \left(\frac{2\pi t}{\tau} \right) \right) S_i^x, \quad (3)$$

where γ_i is the strength of the transverse field on site i . Like the delta kick protocol, we will consider here only the case of a single driven spin. We note that a similar pulse protocol, but with different H_0 , was studied in the context of global drives (all spins driven) to demonstrate the existence of resonant scars [47].

For both drive protocols, we have used the time-dependent $\langle S_i^x \rangle$ and onsite von Neumann entanglement entropy to identify regimes where the driven spin either collectively thermalizes with the rest of the spins, as in Figs. 1(c) and 1(e), or essentially disentangles itself from the remainder of the spins as in Figs. 1(d) and 1(f). The latter case serves as an example of a system that is locally kept athermal (or “cold”) by driving, whereas the rest of the system “heats up” and thermalizes. In the rest of the paper we will explore these phenomena further.

II. FLOQUET AND REAL-SPACE PICTURE OF THERMALIZATION

In this section we discuss both the Floquet (“quasienergy”) space and local (real-space) picture of the phenomena shown in Fig. 1 by placing their behavior in the context of the familiar picture of QMBS. We make the notion of the Floquet quasienergy spectrum precise and clarify how it assumes the role of eigenenergies of the time-independent Hamiltonian, where identification of an isolated manifold with large overlap on the initial state revealed the existence of QMBS [14,15].

A. Floquet Hamiltonian and Floquet overlap profile

For stroboscopic times, defined to be any time which is an integer multiple of the drive periodicity, the unitary Floquet operator completely encodes all information about the time evolution. For a single period, the Floquet operator is given by

$$F(\tau) \equiv e^{-iH_F\tau} = \sum_j e^{-i\epsilon_j\tau} |f_j\rangle \langle f_j|, \quad (4)$$

where H_F is defined to be the effective Hermitian Floquet Hamiltonian, $|f_j\rangle$ is its j th eigenvector and ϵ_j is the corresponding quasienergy. For the two drive protocols introduced

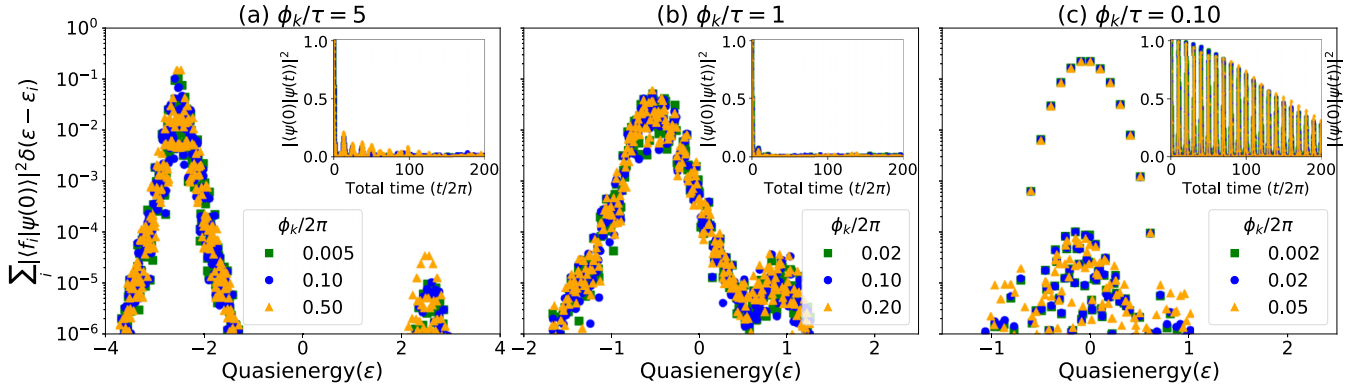


FIG. 2. Floquet overlap profile and (inset) survival probability/Loschmidt echo starting from the fully polarized X state, for representative cases of the local delta kick protocol for $N = 12$ sites with periodic boundary conditions with $J = 1$, $h = 0.1$ and (a) $\phi_k/\tau = 5$, (b) $\phi_k/\tau = 1$, and (c) $\phi_k/\tau = 0.1$. For ease of visualization (and to account for situations with near or exact degeneracies), quasienergies are binned with a spacing of 10^{-2} , and the total overlap on the (nearly) degenerate manifold is reported.

in Eqs. (2) and (3) we have

$$F(\tau) = e^{+i\sum_i \phi_i S_i^x} e^{-iH_0\tau} \quad \text{delta,} \quad (5)$$

$$F(\tau) = e^{-i(H_0 - \sum_i \gamma_i S_i^z)\frac{\tau}{2}} e^{-i(H_0 + \sum_i \gamma_i S_i^z)\frac{\tau}{2}} \quad \text{square.} \quad (6)$$

Knowing $|f_j\rangle$ and ϵ_j and hence $c_j \equiv \langle f_j | \psi(0) \rangle$, enables inference of many properties of the dynamics, for example, the survival probability (Loschmidt echo) is

$$|\langle \psi(0) | \psi(n\tau) \rangle|^2 = \sum_{j,k} |c_j|^2 |c_k|^2 e^{-in(\epsilon_j - \epsilon_k)\tau}, \quad (7)$$

where $n \geq 0$ is an integer. Since the quasienergies typically have spacings that statistically resemble those that arise from a random matrix, this quantity generally goes to zero in the long-time limit by virtue of the superposition of the (almost) random phases. However, this is not always the case—a regularity of the quasienergy spacings for states with dominant $|c_i|$ leads to robust revivals of the survival probability and other observables.

The quasienergies (eigenenergies of H_F) of the driven system play the role analogous to energies of the corresponding undriven system. The overlap of the initial state on to the eigenvectors of the Floquet operator illuminates which states participate in the time evolution of the system. We thus use the plot of $|c_j|^2$ as a function of ϵ_j as a diagnostic tool and refer to it as the “Floquet overlap profile,” as in Figs. 2 and 3. To smoothen the appearance of certain features in the plots, especially in situations with exactly (or nearly) degenerate quasienergies, we divide the quasienergy space into small bins and report the total overlap of all states in the bin.

B. Delta kick

Consider first the case of the local delta kick. On performing a Baker-Campbell-Hausdorff (BCH) expansion of Eq. (5), the Floquet Hamiltonian, to lowest order in the kick strength is

$$H_F^{(0)} = H_0 - \frac{\phi_k}{\tau} S_k^x, \quad (8)$$

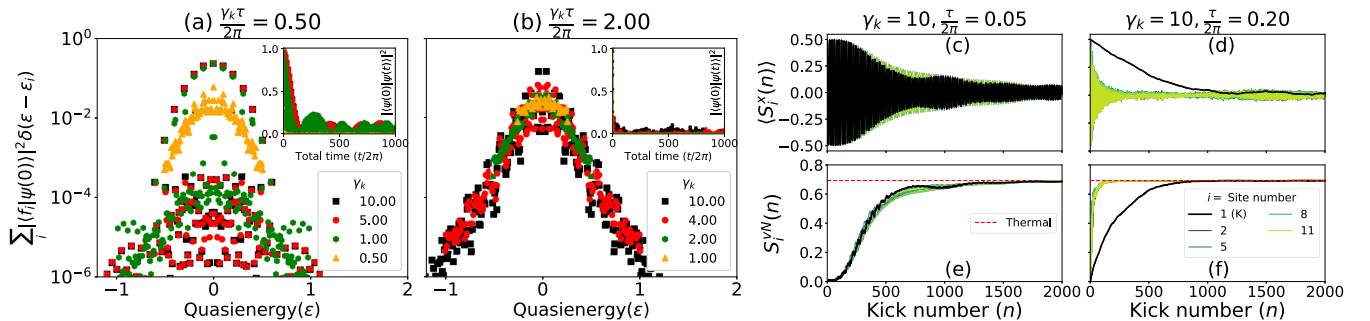


FIG. 3. Panels (a) and (b) show the Floquet overlap profile and (inset) survival probability/Loschmidt echo starting from the $|X\rangle$ state, for representative parameters of the local square pulse protocol for $N = 12$ sites with periodic boundary conditions and $J = 1$, $h = 0.1$. $\gamma_k \tau / 2\pi$ was fixed to the value of (a) 0.50 and (b) 2, while individually varying γ_k and τ . The value in (b) satisfies the resonant condition, see text. Quasienergies are binned with a spacing of 10^{-2} , and the total overlap on the (nearly) degenerate manifold is reported. Panels (c) and (d) show $\langle S_i^x(t) \rangle$ and panels (e) and (f) show the von Neumann entanglement entropy $S_i^{vn}(t)$ for all sites (i) for the cases of $J = 1$, $h = 1$ and [(c) and (e)] $\gamma_k = 10$, $\tau / 2\pi = 0.05$ and [(d) and (f)] $\gamma_k = 10$, $\tau / 2\pi = 0.20$. Panels (c) and (e) show that a single site drive is sufficient to thermalize all the sites. Panels (d) and (f) show slow relaxation of local properties at the driven site due to the resonant condition. Label K is used to indicate the driven site.

as shown in Appendix A. Physically, one can think of the second term as a local magnetic field of strength ϕ_k/τ in the x direction, a viewpoint that will be useful for interpreting the numerical results in the next section.

The mathematical form of Eq. (8) suggests that the Floquet overlap profile and survival probability must be approximately a function of ϕ_k/τ . In Fig. 2 we explore the validity of this assertion by plotting the Floquet overlap profile (main panels) and the Loschmidt echo (inset) for three representative values of ϕ_k/τ showing multiple ϕ_k for each. We find that, for the range of ϕ_k/τ plotted here, our data collapse nicely on top of each other, especially for lower values of ϕ_k . Expectedly, this data collapse begins to break down for large ϕ_k due to the presence of higher-order terms in the Floquet Hamiltonian. (Also note that $\phi_k = 2\pi \times$ integer is special and corresponds to the situation where there is no kick.)

We now explain the trends seen in Fig. 2. If there were no H_0 , then the Floquet quasienergies are $-\phi_k/2\tau$ and $+\phi_k/2\tau$, which correspond to Floquet eigenvectors that have $S_k^x = +1/2$ and $S_k^x = -1/2$ respectively. (The $|X\rangle$ state has overlap only onto the manifold of states with $S_k^x = +1/2$.) When H_0 is present, but ϕ_k/τ is large, S_k^x is not an exact integral of motion, just an approximate one. This situation can be viewed as the realization of weak HSF, two weakly coupled fragments (with $S_k^x \approx \pm 1/2$) appear in Hilbert space. The $|X\rangle$ state now has overlap with both fragments, the larger overlaps come from states with $S_k^x \approx +1/2$. Importantly, the Floquet overlap profile now has “bands” centered at $\pm\phi_k/2\tau$ which have spread out. When these bands do not overlap, as in Fig. 2(a) which corresponds to the case of $\phi_k/\tau = 5$, the kicked spin is athermal. This local physics is not apparent in the Loschmidt echo, plotted in the inset of Fig. 2(a); this quantity does not show any prominent oscillations and instead decays rapidly. This is not unexpected; the Loschmidt echo is a global property of the state which decays with time because majority of the spins lose coherence. This thermalization of the undriven spins arises due to the absence of any regular structure in the Floquet overlap profile; there is no manifold of states with large overlaps and regular spacing of quasienergies.

On making ϕ_k/τ smaller, the previously separated Floquet bands broaden further and eventually begin to merge with one another, as is seen in Fig. 2(b). When this happens, the driven spin does not act significantly differently from the rest of the spins. This collective thermalization is also corroborated by the results in Fig. 1. When the local delta kick is weakened even further, a long thermalization scale emerges due to the vicinity to a “perfect scar” since the $|X\rangle$ state is in the null space of the staggered Heisenberg term—it has a decomposition onto the tower of $2(N/2) + 1 = N + 1$ states. The Floquet overlap profile for $\phi_k/\tau = 0.1$ in Fig. 2(c) demonstrates this very clearly, the quasienergy spacing between states with nonzero overlap is h and it arises from the Zeeman splitting of the embedded ferromagnet.

C. Symmetric square pulse

The Floquet framework, coupled with either the BCH expansion of the participating operators or the Floquet-Magnus (F-M) expansion, offers a way to understand, and hence engineer, the lifetime of QMBS states. For example, consider a

driven spin with a kick that alternates in sign during one time period. In the limit of extremely rapid driving (high frequency driving), the kicks of opposite sign “effectively cancel out” and the system is essentially undriven. Hence, the frequency and strength of the drive can be used as knobs for controlling decoherence times—higher frequency and weaker drive strengths favor longer decoherence times.

The symmetric square pulse that we consider here also alternates in sign in one time period. As shown in Appendix B, the Floquet Hamiltonian for the local square pulse to lowest order is

$$\begin{aligned}
 H_F^{(0)} = & (-1)^k \left[S_k^x S_{k+1}^x + \frac{2 \sin\left(\frac{\gamma_k \tau}{2}\right)}{\gamma_k \tau} (S_k^y S_{k+1}^y + S_k^z S_{k+1}^z) \right. \\
 & \left. - \frac{2(1 - \cos\left(\frac{\gamma_k \tau}{2}\right))}{\gamma_k \tau} (S_k^z S_{k+1}^y - S_k^y S_{k+1}^z) \right] \\
 & - (-1)^k \left[S_{k-1}^x S_k^x + \frac{2 \sin\left(\frac{\gamma_k \tau}{2}\right)}{\gamma_k \tau} (S_{k-1}^y S_k^y + S_{k-1}^z S_k^z) \right. \\
 & \left. - \frac{2(1 - \cos\left(\frac{\gamma_k \tau}{2}\right))}{\gamma_k \tau} (S_{k-1}^z S_k^y - S_{k-1}^y S_k^z) \right] \\
 & - \frac{2h}{\gamma_k \tau} \left(\sin\left(\frac{\gamma_k \tau}{2}\right) S_k^z + \left(1 - \cos\left(\frac{\gamma_k \tau}{2}\right)\right) S_k^y \right) \\
 & + \sum_{\substack{i=1 \\ i \neq (k-1, k)}}^N (-1)^i \mathbf{S}_i \cdot \mathbf{S}_{i+1} - h \sum_{\substack{i=1 \\ i \neq k}}^N S_i^z. \tag{9}
 \end{aligned}$$

Two important takeaways from Eq. (9) are (1) $H_F^{(0)}$ just depends on $\gamma_k \tau$, a finding confirmed by the (approximate) data collapse seen in the Floquet overlap profile in Figs. 3(a) and 3(b) and (2) there are special values of drive frequency and strength—the “resonant condition” [47] ($\gamma_k \tau = 4\pi \times$ integer)—where the system is locally athermal, a phenomenon referred to as dynamic freezing. Since the F-M expansion is most accurate at high drive frequency ($\gamma_k \tau \ll 1$), we expect the Floquet Hamiltonian to be well approximated by $H_F^{(0)}$ only in that regime.

At high frequencies ($\gamma_k \tau \ll 1$), the drive is effectively rendered ineffective and $H_F^{(0)} \approx H_0$. In this regime, the $|X\rangle$ state is an almost perfect QMBS—it shows coherent oscillations in the survival probability and other observables (not shown). At intermediate frequencies $\gamma_k \tau \sim 1$, the Floquet overlap profile, as in Fig. 3(a), continues to show the characteristic manifold associated with QMBS and the associated superspin. However, there are now subdominant modes that are important for thermalization at long times. (The data collapse for fixed $\gamma_k \tau$ is most accurate for large γ_k and small τ .) Figures 3(c) and 3(e) shows the time-dependent value of the onsite $\langle S_i^y \rangle$ and the von Neumann entanglement entropy; there are collective coherent oscillations in both quantities at short times but eventual relaxation at long times. Thus, single site driving is sufficient to thermalize all the sites including the driven site, which is reminiscent of the behavior of the delta-kicked system for intermediate ϕ_k/τ .

Figures 3(b), 3(d), and 3(f) correspond to the case of a resonant frequency. The Floquet overlap profile shows that the characteristic QMBS manifold is lost; instead, the situation

resembles that of the delta-kick for large ϕ_k/τ . Unlike the case of a global drive at resonance [47], the locally driven spin is not entirely frozen out but it does relax significantly slowly compared to the other undriven spins. This ruining of dynamic freezing is caused by higher-order terms in the F-M expansion of H_F , which some of us have pursued in detail elsewhere [52].

III. REAL-SPACE, REAL-TIME PROFILE OF THERMALIZATION

In this section we take a more refined look at the real-space, real-time picture of thermalization for a chain with open boundaries, where the central site is subject to a periodic delta kick. We simulate the short-time dynamics of a $N = 51$ site system with the matrix product state– (MPS) based time-evolving block decimation (TEBD) algorithm [59] employing a maximum bond dimension of 400. To address (extremely) long-time behavior, we simulate a much smaller system size of $N = 13$ with exact diagonalization.

More generally we find that for a given set of drive parameters, the Floquet dynamics can be sensitive to N , an issue that we address in Appendix C. (That said, we have observed that the $N = 31$ open chain exhibits similar qualitative behavior as $N = 51$ for the same drive parameters.)

A. Short-time dynamics with TEBD

To visualize dynamics of $N = 51$ spins in both space and time we construct a “space-time” plot, as in Fig. 4, space is shown horizontally and time is shown vertically and the color represents the value of the quantity being investigated. Since the system is initially prepared in the $|X\rangle$ state, the von Neumann entanglement entropy of each spin is exactly zero to begin with. As time progresses, the entanglement spreads out in a “cone” and distant regions begin to feel the effects of the periodic kicking. This can be seen prominently in Fig. 4 for $\tau/2\pi = 0.13$ for both $\phi_k/2\pi = 0.1$ [Fig. 4(a)] and $\phi_k/2\pi = 0.5$ [Fig. 4(b)] at short times. (A time step of $\tau/20$ was used for the TEBD simulations, smaller time steps gave similar results.) After this initial phase, the regions around the central spin show a prominent dip in their entanglement—they get cold after an initial phase of heating up—which appears as two blue lobes around the kicked spin. These regions eventually heat up at longer times, more generally, the plots show oscillatory behavior both in space and time [60] We also note that similar observations, albeit for a different model and observables, have been reported recently in Ref. [61]. (Note that the system is not inversion symmetric because of the alternating J 's, but the plot of the entanglement entropy appears to be approximately symmetric about the central site.) As pointed out earlier in Fig. 1, the driven site acts as a cold spot for $\phi_k/2\pi = 0.5$ —visually it appears as a blue vertical line in the space-time plot in Fig. 4(b).

To further probe how the driven spin behaves relative to the other (undriven) ones, we plot $\langle S_i^y \rangle$ for the two parameter sets in Figs. 4(c) and 4(d). On the timescale plotted, $\langle S_i^y \rangle$ shows collective revivals but they decay with time. Many of its features, at short times, can be understood without worrying about the interactions (J terms). For example, for small ϕ_k ,

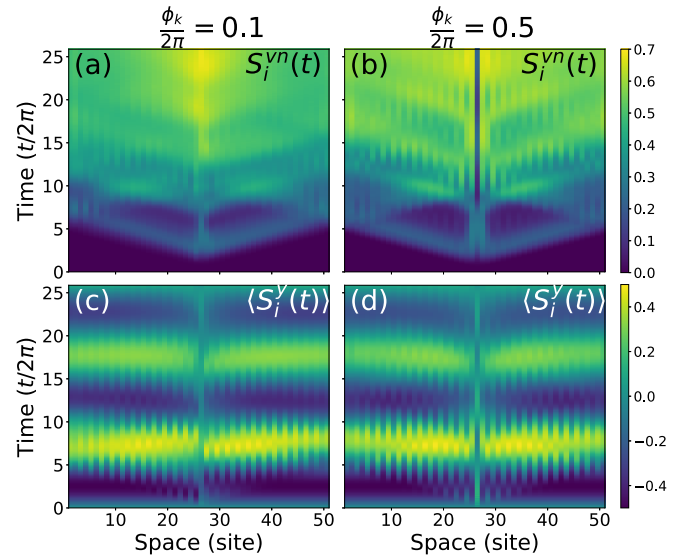


FIG. 4. Space-time thermalization profile for a $N = 51$ site delta-kicked staggered Heisenberg chain with open boundary conditions, showing the von Neumann entanglement entropy [(a) and (b)] $S_i^{vn}(t)$ of each site and [(c) and (d)] $\langle S_i^y(t) \rangle$. Space and time correspond to the horizontal and vertical axes respectively and the color represents the value of the physical quantity. Results are for $J = 1$, $h = 0.1$, $\tau/2\pi = 0.13$ and [(a) and (c)] $\phi_k/2\pi = 0.1$ and [(b) and (d)] $\phi_k/2\pi = 0.5$.

following Eq. (8) the additional local effective magnetic field contribution along the x direction is small. Thus the driven spin, like the other spins, precesses predominantly in the $x - y$ plane, i.e., the axis about which it precesses is close to the direction of the applied field (z direction). Since the superspin picture is intact, the driven spin is (largely) in phase with the others; this can be seen for the case of $\phi_k/2\pi = 0.1$ in Fig. 4(c). This picture changes when the drive strength is large—the axis about which the driven spin precesses is now much closer to the x axis; however, the axis for the other spins is unaffected. Since the starting state is the $|X\rangle$ state, with only a small component of the spin orthogonal to the axis of precession, the strength of the oscillations in $\langle S_i^y(t) \rangle$ are weak. These oscillations are also out of phase with respect to those of the other spins, as can be seen in Fig. 4(d).

For the $N = 51$ site chain, we also study the case of effectively weaker kicks by fixing the kick frequency to a value 10 times smaller, i.e., $\frac{\tau}{2\pi} = 1.30$. A time step of $\tau/200$ was used for the TEBD calculations, i.e., the same overall time step as that for the previously discussed cases. Figure 5(a) shows the time dependence of the von Neumann entanglement entropy for the driven spin for a few representative values of ϕ_k for this value of τ . After an initial stage of entanglement growth, the entanglement entropy of the kicked spin [and other spins as seen in the space-time plot in Figs. 5(b) and 5(c)] fluctuates about a nonzero value; the value of this short-time “plateau” and the strength of the oscillations both grow with ϕ_k . The fact that this value is far from the thermal expectation of $\ln 2$, and that it is similar for all spins, reflects the resilience of the superspin to local driving, at least at short times.

Figures 5(d) and 5(e) show $\langle S_i^y(t) \rangle$ for the two values of ϕ_k . We observe robust revivals in both cases on the timescale of

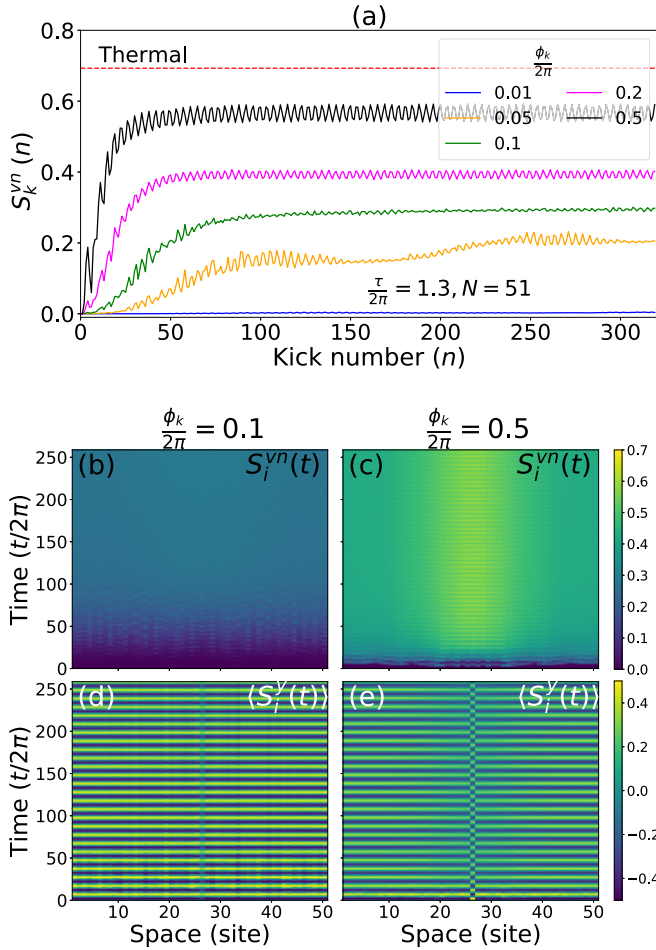


FIG. 5. Panel (a) shows TEBD results for the time-dependent von Neumann entanglement entropy of the central kicked site for the $N = 51$ open chain and $\tau/2\pi = 1.30$ and a few representative values of $\phi_k/2\pi$. The red dashed line corresponds to the maximal entropy of $\ln 2$. For the same system and drive frequency as in (a), the lower panels show space-time plots of the von Neumann entanglement entropy [(b) and (c)] and the expectation value of $\langle S_i^y(t) \rangle$ [(d) and (e)] for two values of drive strength $\phi_k/2\pi = 0.1$ [(b) and (d)] and $\phi_k/2\pi = 0.5$ [(c) and (e)].

the simulation, and the in-phase versus out-of-phase behavior of the driven spin closely parallels that seen for the case of lower τ in Fig. 4. However, for $\phi_k = \pi$, the driven spin is not decoupled or “cold,” on the contrary it is slightly more entangled compared to rest of the spins.

B. Long-time dynamics with exact diagonalization

Unfortunately, the TEBD simulations reveal information only about the short-time dynamics. Thus it is unclear whether our observations correspond to truly athermal or just transient prethermal behavior. To address this issue, we have explored the possibility of similar trends for smaller systems where full diagonalization of the Floquet operator is possible which, in turn, allows arbitrary stroboscopic times to be accessed.

Figures 6(a) and 6(b) show our results for the von Neumann entanglement entropy of the kicked site on a logarithmic time grid at short and long times (spanning many orders

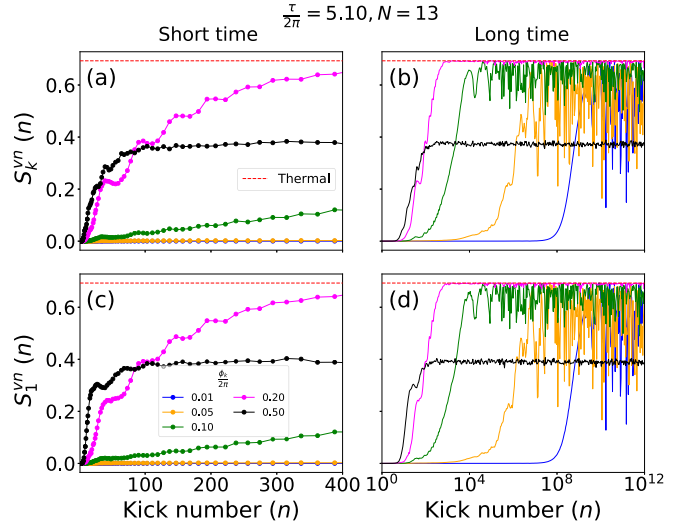


FIG. 6. Exact diagonalization results for the time-dependent von Neumann entanglement entropy of the central kicked site [(a) and (b)] and the leftmost boundary spin [site 1; (c) and (d)] for the $N = 13$ open chain for $\tau/2\pi = 5.10$ and a few representative values of $\phi_k/2\pi$. The parameters used were $J = 1$, $h = 0.1$. The red dashed line corresponds to the maximal entropy of $\ln 2$. Panels (a) and (c) correspond to short timescales and are plotted on a linear axis and panels (b) and (d) correspond to long timescales plotted on a log axis. Markers correspond to stroboscopic times at which the quantity was evaluated, the connecting lines are guides to the eye.

of magnitude) respectively for the $N = 13$ open chain and $\tau/2\pi = 5.10$. Note that the value of τ was chosen to be different in comparison to the $N = 51$ case. (The sensitivity of the Floquet dynamics on system size is discussed in Appendix C.) Figures 6(c) and 6(d) show that the leftmost boundary spin closely follows the central/kicked spin at both short and long times like the other spins in the system (not shown).

At short times, the dynamics of the small chain qualitatively resembles that of the larger chain. There are some differences however, for example, the entropy curves for $\phi_k/2\pi = 0.2$ and $\phi_k/2\pi = 0.5$ cross. At much longer times, well beyond those accessible to TEBD, the entropy crosses over to significantly higher values, but not always the maximal value of $\ln 2 \approx 0.693$. This is most prominently seen for the case of $\phi_k = \pi$ where the value is relatively constant (at approximately 0.4) over multiple decades of time. As expected, the timescale at which the rapid crossover from low to high entanglement occurs is inversely proportionate to ϕ_k . Additionally, for small values of ϕ_k , we observe visibly large fluctuations even at very long times indicating some remnant coherence, a feature that we intend to explore more systematically elsewhere. The deviation from the maximal entropy suggests the possible existence of truly athermal behavior or alternatively, a very long prethermal timescale [62], for some of the parameter sets studied here.

We emphasize that the existence of finite entanglement plateaus, for example those seen in Figs. 5 and 6, is considerably different from the case where the system is not driven. In the latter case, the system always remains in a (zero entanglement) product state at all times during the evolution. As noted earlier, when there is no drive, the interactions are

rendered ineffective due to the choice of initial condition [24]. However, in the weakly driven case, interactions facilitate the initial period of entanglement growth and the system reaches a quasi-steady state where it collectively remains as a superspin for a timescale that is ϕ_k dependent. In the extremely long-time limit, this superspin typically, but not always, loses its coherence completely leading to thermalization.

The possible explanation of this effect is rooted in a consideration of the Floquet Hamiltonian. In the limit that ϕ_k/τ is small, the zeroth order term may be inadequate for even a qualitatively accurate description [52]. Instead, one must consider higher-order terms which may either compete or collaborate to renormalize the effective magnetic field that the kicked site experiences, as seen in Eqs. (A2a) and (A2b). If the effective field is driven to a small value, then thermalization is slow. Consequently, the system may also exhibit a thermalization rate that sensitively depends on the size of the system N . On the one hand, the periodic kick has the effect of disturbing the coherently precessing spins, so larger N leads to longer times for the entire system to feel the disturbance. On the other hand, larger N also means there are more channels to exchange energy which could lead to faster thermalization. These competing effects manifest themselves in nontrivial ways and we have addressed this issue numerically in Appendix C. In particular, we have provided evidence of nonmonotonic (with N) effects with the help of Figs. 7 and 8.

IV. CONCLUSION

In summary, we have explored the different dynamical regimes of a locally driven staggered (alternating sign) Heisenberg spin chain for local drive protocols that should be experimentally accessible. For the X -polarized initial state, the driven spin crosses over from full thermalization to athermal dynamics, effectively decoupling from the rest of the spins, as the rest of the system thermalizes. Both drive protocols showed this effect, and the numerical observations were explained within the framework of the lowest-order Floquet Hamiltonian. We also discovered parametric regimes where a quasi-steady state is reached after a period of initial entanglement growth, with collective oscillations, suggesting the resilience of the superspin picture for effectively weak drives. An important conceptual outcome is that both the local and Floquet-space pictures are complementary for understanding the mechanism by which the system thermalizes or fails to do so. More generally, our analyses also potentially carry over to the case of periodic drives with spatial deformed Hamiltonians [63].

Given the simplicity of the model and drive protocols investigated here, we believe these predictions can be tested. There are now many synthetic realizations of spin and Bose Hubbard systems [64]: in addition to Rydberg atoms, ytterbium-171 has been recently used to realize an effective transverse Ising model [65] and hyperfine states of lithium realize XXZ models with tunable anisotropy [66]. Our observation of the local breakdown of thermalization in an otherwise thermal system for a certain initial state provides a nontrivial mechanism for protecting information in a

periodically driven system and sheds light on the novel behavior of dynamics of many-body entanglement.

ACKNOWLEDGMENTS

We thank K. Lee for useful discussions in the initial stages of the project and for a previous collaboration. R.M., P.S., and H.J.C. acknowledge support from Grant No. NSF DMR-2046570 and Florida State University (FSU) and the National High Magnetic Field Laboratory. The National High Magnetic Field Laboratory is supported by the National Science Foundation through Grants No. DMR-1644779 and No. DMR-2128556 and by the state of Florida. A.P. and B.M. were funded by the European Research Council (ERC) under the European Union's Horizon 2020 research and innovation programme (Grant No. 853368). We also thank the Planck cluster and the Research Computing Center (RCC) at FSU for computing resources. The MPS-based TEBD calculations were based on the ITensor library [67].

APPENDIX A: H_F FOR THE PERIODIC DELTA KICK PROTOCOL

In this Appendix we derive an approximation for H_F for the periodic delta kick protocol with the help of the truncated BCH expansion applied to Eq. (5).

Set $X \equiv i\phi_k S_k^x$, $Y \equiv -iH_0\tau$ and $Z \equiv -iH_F\tau$, then H_F is given by

$$H_F = \frac{iZ}{\tau} = \frac{i}{\tau} \ln(e^X e^Y). \quad (\text{A1})$$

Defining $H_F \equiv \sum_n H_F^{(n)}$, we determine $H_F^{(n)}$ using the BCH formula and get

$$H_F^{(0)} = \frac{i}{\tau} (X + Y) = H_0 - \frac{\phi_k}{\tau} S_k^x, \quad (\text{A2a})$$

$$\begin{aligned} H_F^{(1)} &= \frac{i}{\tau} \frac{[X, Y]}{2} \\ &= \frac{\phi_k}{2} \left((-1)^k (S_{k-1}^y S_k^z + S_k^y S_{k+1}^z - S_{k-1}^z S_k^y - S_k^z S_{k+1}^y) \right. \\ &\quad \left. - h S_k^y \right). \end{aligned} \quad (\text{A2b})$$

APPENDIX B: H_F FOR THE SQUARE PULSE PROTOCOL

In this Appendix we provide a detailed calculation of the stroboscopic H_F for the square pulse protocol using the F-M expansion in a rotating frame. The F-M method yields H_F as a perturbative expansion in inverse drive frequency (τ). However, transition to a rotating frame automatically ensures an infinite-order resummation in τ . Thus, we obtain a series expansion of H_F in inverse drive amplitude ($1/\gamma_k$) where all the terms are resummed in τ [68–71]. This extends the validity of H_F to the low-drive-frequency regime but limits it to the high-drive-amplitude regime.

As mentioned in the text, the local drive at the k th site is given by $H_D(t) = \gamma_k \text{Sgn}(\sin(\omega t)) S_k^x$ with $\omega = 2\pi/\tau$. It is convenient to transform the time-dependent Hamiltonian $H(t) = H_0 + H_D(t)$ to a rotating frame as follows:

$$H_{\text{rot}}(t) = W^\dagger H(t) W - iW^\dagger \partial_t W, \quad (\text{B1})$$

where

$$W(t) = e^{-i \int_0^t dt' H_D(t')} = e^{-i\theta(t)S_k^x} \quad (\text{B2})$$

and

$$\theta(t) = \gamma_k t \Theta(\tau/2 - t) + \gamma_k (\tau - t) \Theta(t - \tau/2). \quad (\text{B3})$$

This transformation removes the driving term $[H_D(t)]$ from the Hamiltonian in rotating frame $[H_{\text{rot}}(t)]$ and we get

$$\begin{aligned} H_{\text{rot}}(t) &= W^\dagger H_0 W = \mathcal{H}(k-1, k) + \mathcal{H}(k, k+1) \\ &\quad - h(\cos(\theta)S_k^z + \sin(\theta)S_k^y) \\ &\quad + \sum_{\substack{i=1 \\ i \neq (k-1, k)}}^N (-1)^i \mathbf{S}_i \cdot \mathbf{S}_{i+1} - h \sum_{\substack{i=1 \\ i \neq k}}^N S_i^z, \end{aligned} \quad (\text{B4})$$

where

$$\begin{aligned} \mathcal{H}(k, k+1) &= (-1)^k [S_k^x S_{k+1}^x + \cos(\theta)(S_k^y S_{k+1}^y + S_k^z S_{k+1}^z) \\ &\quad - \sin(\theta)(S_k^z S_{k+1}^y - S_k^y S_{k+1}^z)] \end{aligned} \quad (\text{B5})$$

and we have used

$$W^\dagger S_k^z W = \cos(\theta)S_k^z + \sin(\theta)S_k^y, \quad (\text{B6a})$$

$$W^\dagger S_k^y W = -\sin(\theta)S_k^z + \cos(\theta)S_k^y. \quad (\text{B6b})$$

The zeroth-order Floquet Hamiltonian is just the time-averaged $H_{\text{rot}}(t)$ over one time period,

$$\begin{aligned} H_F^{(0)} &= \frac{1}{\tau} \int_0^\tau H_{\text{rot}}(t) dt = \mathcal{H}_F^{(0)}(k-1, k) \\ &\quad + \mathcal{H}_F^{(0)}(k, k+1) + h_F^{(0)}(k) \\ &\quad + \sum_{\substack{i=1 \\ i \neq (k-1, k)}}^N (-1)^i \mathbf{S}_i \cdot \mathbf{S}_{i+1} - h \sum_{\substack{i=1 \\ i \neq k}}^N S_i^z, \end{aligned} \quad (\text{B7})$$

where

$$\begin{aligned} \mathcal{H}_F^{(0)}(k, k+1) &= (-1)^k \left[S_k^x S_{k+1}^x + \frac{2 \sin\left(\frac{\gamma_k \tau}{2}\right)}{\gamma_k \tau} \right. \\ &\quad \times (S_k^y S_{k+1}^y + S_k^z S_{k+1}^z) - \frac{2(1 - \cos\left(\frac{\gamma_k \tau}{2}\right))}{\gamma_k \tau} \\ &\quad \left. \times (S_k^z S_{k+1}^y - S_k^y S_{k+1}^z) \right] \end{aligned} \quad (\text{B8a})$$

$$\begin{aligned} h_F^{(0)}(k) &= -\frac{2h}{\gamma_k \tau} \left[\sin\left(\frac{\gamma_k \tau}{2}\right) S_k^z \right. \\ &\quad \left. + \left(1 - \cos\left(\frac{\gamma_k \tau}{2}\right)\right) S_k^y \right]. \end{aligned} \quad (\text{B8b})$$

APPENDIX C: NONMONOTONIC SYSTEM SIZE DEPENDENCE OF FLOQUET DYNAMICS

In this Appendix we provide numerical evidence for the sensitivity of Floquet dynamics to the system size N . We consider chains with odd N and open boundaries, with the central site being driven/kicked periodically. The spins are initialized, at $t = 0$, to the $|X\rangle$ state.

In Fig. 7 we plot the von Neumann entanglement entropy for the driven (central) site at stroboscopic times for $\phi_k/2\pi =$

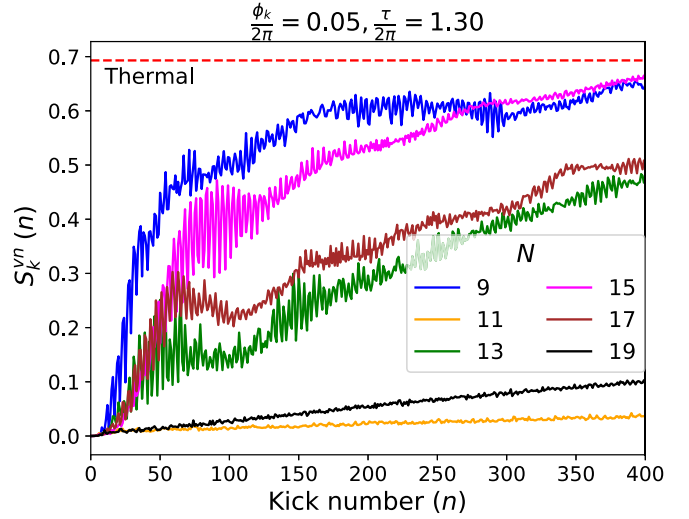


FIG. 7. Time-dependent von Neumann entanglement entropy of the driven (kicked) site, denoted by S_k^{vN} , for chains of length N with open boundary conditions, whose central site is subject to a periodic delta kick. The parameters are $J = 1$, $h = 0.1$, $\frac{\phi_k}{2\pi} = 0.05$, and $\frac{\tau}{2\pi} = 1.30$.

0.05 and $\tau/2\pi = 1.30$ and $J = 1$, $h = 0.1$. The results were obtained with TEBD with a maximum bond dimension of 512, and thus there is no truncation error for $N \leq 19$. The time step was chosen to be small ($\delta t = \tau/200$), such that the TEBD results matched the exact diagonalization results (for $N = 9, 11, 13$) to a high accuracy, throughout the entire time window shown in the plot.

We observe nonmonotonic (with N) trends. The $N = 11$ chain shows almost no change in the entanglement entropy from its initial value of zero, in sharp contrast to the $N = 9$

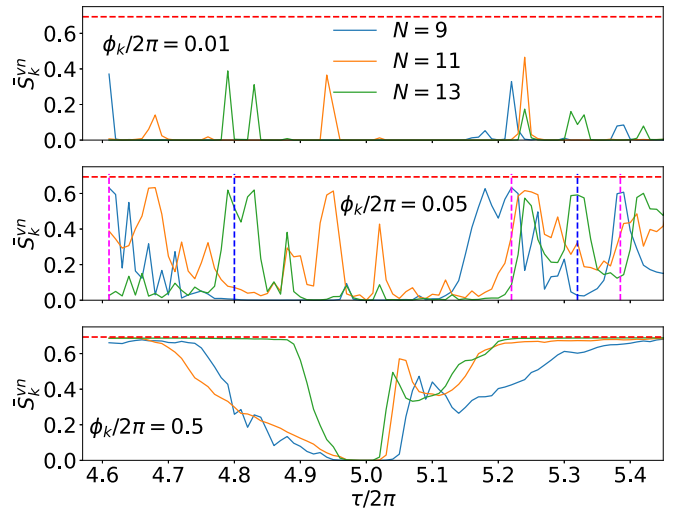


FIG. 8. Entanglement entropy of the kicked site, averaged over first 1000 drive cycles (\bar{S}_k^{vN}) vs $\tau/2\pi$ for three different system sizes. Horizontal red dashed line in each panel denotes the thermal value of entropy ($\ln 2$). Vertical dashed lines in the middle panel are guide to the eye for the cases when the relaxation becomes faster (blue) and slower (magenta) with system size. The parameters are $J = 1$, $h = 0.1$.

case. The time profile then changes again for larger N , the rate of increase of entanglement entropy increases for $N = 13$ and $N = 15$ but then slows down again for $N = 17$ and (more prominently) for $N = 19$.

To further explore this effect, in Fig. 8 we plot the average entanglement entropy of the kicked spin over the first 1000 drive cycles (kicks), for $N = 9, 11, 13$, computed with exact diagonalization. We consider a range of $\tau/2\pi$, in the vicinity of 5.10, in steps of 0.01, and representative values of $\phi_k/2\pi = 0.01, 0.05$, and 0.5 with $J = 1, h = 0.1$. This plotted quantity captures the average (initial) rate of relaxation towards thermal equilibrium—larger values indicate fast approach towards the thermal state and low values indicate slow or no relaxation in the time window of the first 1000 kicks. Note that the case of $\tau/2\pi = 5$ is special given that $h = 0.1$ —it corresponds to half the time period of the precession. This means that the

delta kick is given to a spin when it is in an eigenstate of S_k^x , which has the effect of only contributing a global phase to the time-dependent wave function, which does not disturb the coherent precession of the spins. Thus the state remains a product state for this τ .

For $\phi_k/2\pi = 0.01$ the relaxation is, in general, slow for most τ . However, there are some τ for which the relaxation rate is faster, importantly they occur at different τ for different N . This is confirmed in the middle panel, for $\phi_k/2\pi = 0.05$, the vertical dashed lines indicate situations where the relaxation becomes prominently faster or slower with increasing system size. The bottom panel shows our results for $\phi_k/2\pi = 0.5$. Once again there is generically a strong dependence on N ; however, there are regimes (for example, $\tau/2\pi \approx 5.1$) where the relaxation rates for the three sizes shown here are coincidentally similar.

-
- [1] J. M. Deutsch, Quantum statistical mechanics in a closed system, *Phys. Rev. A* **43**, 2046 (1991).
- [2] M. Srednicki, Chaos and quantum thermalization, *Phys. Rev. E* **50**, 888 (1994).
- [3] M. Rigol, V. Dunjko, and M. Olshanii, Thermalization and its mechanism for generic isolated quantum systems, *Nature (London)* **452**, 854 (2008).
- [4] R. V. Jensen and R. Shankar, Statistical behavior in deterministic quantum systems with few degrees of freedom, *Phys. Rev. Lett.* **54**, 1879 (1985).
- [5] L. D. Landau and E. M. Lifshitz, *Statistical Physics*, 3rd ed. (Butterworth-Heinemann, Oxford, 1980).
- [6] D. M. Basko, I. L. Aleiner, and B. L. Altshuler, Metal-insulator transition in a weakly interacting many-electron system with localized single-particle states, *Ann. Phys.* **321**, 1126 (2006).
- [7] A. Pal and D. A. Huse, Many-body localization phase transition, *Phys. Rev. B* **82**, 174411 (2010).
- [8] V. Oganesyan and D. A. Huse, Localization of interacting fermions at high temperature, *Phys. Rev. B* **75**, 155111 (2007).
- [9] R. Nandkishore and D. A. Huse, Many-body localization and thermalization in quantum statistical mechanics, *Annu. Rev. Condens. Matter Phys.* **6**, 15 (2015).
- [10] D. A. Abanin, E. Altman, I. Bloch, and M. Serbyn, *Colloquium: Many-body localization, thermalization, and entanglement*, *Rev. Mod. Phys.* **91**, 021001 (2019).
- [11] E. J. Heller, Bound-state eigenfunctions of classically chaotic Hamiltonian systems: Scars of periodic orbits, *Phys. Rev. Lett.* **53**, 1515 (1984).
- [12] O. Vafek, N. Regnault, and B. A. Bernevig, Entanglement of exact excited eigenstates of the Hubbard model in arbitrary dimension, *SciPost Phys.* **3**, 043 (2017).
- [13] N. Shiraishi and T. Mori, Systematic construction of counterexamples to the eigenstate thermalization hypothesis, *Phys. Rev. Lett.* **119**, 030601 (2017).
- [14] C. J. Turner, A. A. Michailidis, D. A. Abanin, M. Serbyn, and Z. Papić, Weak ergodicity breaking from quantum many-body scars, *Nat. Phys.* **14**, 745 (2018).
- [15] C. J. Turner, A. A. Michailidis, D. A. Abanin, M. Serbyn, and Z. Papić, Quantum scarred eigenstates in a Rydberg atom chain: Entanglement, breakdown of thermalization, and stability to perturbations, *Phys. Rev. B* **98**, 155134 (2018).
- [16] S. Moudgalya, S. Rachel, B. A. Bernevig, and N. Regnault, Exact excited states of nonintegrable models, *Phys. Rev. B* **98**, 235155 (2018).
- [17] S. Moudgalya, N. Regnault, and B. A. Bernevig, Entanglement of exact excited states of Affleck-Kennedy-Lieb-Tasaki models: Exact results, many-body scars, and violation of the strong eigenstate thermalization hypothesis, *Phys. Rev. B* **98**, 235156 (2018).
- [18] C.-J. Lin and O. I. Motrunich, Exact quantum many-body scar states in the Rydberg-blockaded atom chain, *Phys. Rev. Lett.* **122**, 173401 (2019).
- [19] V. Khemani, C. R. Laumann, and A. Chandran, Signatures of integrability in the dynamics of Rydberg-blockaded chains, *Phys. Rev. B* **99**, 161101(R) (2019).
- [20] K. Bull, I. Martin, and Z. Papić, Systematic construction of scarred many-body dynamics in 1D lattice models, *Phys. Rev. Lett.* **123**, 030601 (2019).
- [21] M. Schecter and T. Iadecola, Weak ergodicity breaking and quantum many-body scars in spin-1 XY magnets, *Phys. Rev. Lett.* **123**, 147201 (2019).
- [22] S. Ok, K. Choo, C. Mudry, C. Castelnuovo, C. Chamon, and T. Neupert, Topological many-body scar states in dimensions one, two, and three, *Phys. Rev. Res.* **1**, 033144 (2019).
- [23] K. Lee, R. Melendrez, A. Pal, and H. J. Changlani, Exact three-colored quantum scars from geometric frustration, *Phys. Rev. B* **101**, 241111 (2020).
- [24] K. Lee, A. Pal, and H. J. Changlani, Frustration-induced emergent Hilbert space fragmentation, *Phys. Rev. B* **103**, 235133 (2021).
- [25] P. A. McClarty, M. Haque, A. Sen, and J. Richter, Disorder-free localization and many-body quantum scars from magnetic frustration, *Phys. Rev. B* **102**, 224303 (2020).
- [26] J. Wildeboer, A. Seidel, N. S. Srivatsa, A. E. B. Nielsen, and O. Erten, Topological quantum many-body scars in quantum dimer models on the kagome lattice, *Phys. Rev. B* **104**, L121103 (2021).
- [27] K. Pakrouski, P. N. Pallegar, F. K. Popov, and I. R. Klebanov, Many-body scars as a group invariant sector of Hilbert space, *Phys. Rev. Lett.* **125**, 230602 (2020).

- [28] B. van Voorden, J. Minář, and K. Schoutens, Quantum many-body scars in transverse field Ising ladders and beyond, *Phys. Rev. B* **101**, 220305(R) (2020).
- [29] W.-L. You, Z. Zhao, J. Ren, G. Sun, L. Li, and A. M. Oleś, Quantum many-body scars in spin-1 Kitaev chains, *Phys. Rev. Res.* **4**, 013103 (2022).
- [30] E. Chertkov and B. K. Clark, Motif magnetism and quantum many-body scars, *Phys. Rev. B* **104**, 104410 (2021).
- [31] Y. Kuno, T. Mizoguchi, and Y. Hatsugai, Flat band quantum scar, *Phys. Rev. B* **102**, 241115(R) (2020).
- [32] E. S. Ma, K. L. Zhang, and Z. Song, Steady helix states in a resonant XXZ Heisenberg model with Dzyaloshinskii-Moriya interaction, *Phys. Rev. B* **106**, 245122 (2022).
- [33] P. Sharma, K. Lee, and H. J. Changlani, Multimagnon dynamics and thermalization in the $s = 1$ easy-axis ferromagnetic chain, *Phys. Rev. B* **105**, 054413 (2022).
- [34] S. Pilatowsky-Cameo, D. Villaseñor, M. A. Bastarrachea-Magnani, S. Lerma-Hernández, L. F. Santos, and J. G. Hirsch, Ubiquitous quantum scarring does not prevent ergodicity, *Nat. Commun.* **12**, 852 (2021).
- [35] M. Serbyn, D. A. Abanin, and Z. Papić, Quantum many-body scars and weak breaking of ergodicity, *Nat. Phys.* **17**, 675 (2021).
- [36] A. Chandran, T. Iadecola, V. Khemani, and R. Moessner, Quantum many-body scars: A quasiparticle perspective, *Annu. Rev. Condens. Matter Phys.* **14**, 443 (2023).
- [37] S. Dooley, Robust quantum sensing in strongly interacting systems with many-body scars, *PRX Quantum* **2**, 020330 (2021).
- [38] K. K. W. Ma, A. Volya, and K. Yang, Eigenstate thermalization and disappearance of quantum many-body scar states in weakly interacting fermion systems, *Phys. Rev. B* **106**, 214313 (2022).
- [39] P. Sala, T. Rakovszky, R. Verresen, M. Knap, and F. Pollmann, Ergodicity breaking arising from Hilbert space fragmentation in dipole-conserving Hamiltonians, *Phys. Rev. X* **10**, 011047 (2020).
- [40] V. Khemani, M. Hermele, and R. Nandkishore, Localization from Hilbert space shattering: From theory to physical realizations, *Phys. Rev. B* **101**, 174204 (2020).
- [41] A. Khudorozhkov, A. Tiwari, C. Chamon, and T. Neupert, Hilbert space fragmentation in a 2D quantum spin system with subsystem symmetries, *SciPost Phys.* **13**, 098 (2022).
- [42] S. Moudgalya and O. I. Motrunich, Hilbert space fragmentation and commutant algebras, *Phys. Rev. X* **12**, 011050 (2022).
- [43] B. Mukherjee, S. Nandy, A. Sen, D. Sen, and K. Sengupta, Collapse and revival of quantum many-body scars via Floquet engineering, *Phys. Rev. B* **101**, 245107 (2020).
- [44] H. Zhao, J. Vovrosh, F. Mintert, and J. Knolle, Quantum many-body scars in optical lattices, *Phys. Rev. Lett.* **124**, 160604 (2020).
- [45] D. Bluvstein, A. Omran, H. Levine, A. Keesling, G. Semeghini, S. Ebadi, T. T. Wang, A. A. Michailidis, N. Maskara, W. W. Ho *et al.*, Controlling quantum many-body dynamics in driven Rydberg atom arrays, *Science* **371**, 1355 (2021).
- [46] B. Mukherjee, A. Sen, D. Sen, and K. Sengupta, Dynamics of the vacuum state in a periodically driven Rydberg chain, *Phys. Rev. B* **102**, 075123 (2020).
- [47] A. Haldar, D. Sen, R. Moessner, and A. Das, Dynamical freezing and scar points in strongly driven Floquet matter: Resonance vs emergent conservation laws, *Phys. Rev. X* **11**, 021008 (2021).
- [48] D. Thuberg, S. A. Reyes, and S. Eggert, Quantum resonance catastrophe for conductance through a periodically driven barrier, *Phys. Rev. B* **93**, 180301(R) (2016).
- [49] A. Agarwala and D. Sen, Effects of local periodic driving on transport and generation of bound states, *Phys. Rev. B* **96**, 104309 (2017).
- [50] F. Hübner, C. Dauer, S. Eggert, C. Kollath, and A. Sheikhan, Floquet-engineered pair and single-particle filters in the Fermi-Hubbard model, *Phys. Rev. A* **106**, 043303 (2022).
- [51] H. Bethe, Zur theorie der metalle, *Z. Phys.* **71**, 205 (1931).
- [52] B. Mukherjee, R. Melendrez, M. Szyniszewski, H. J. Changlani, and A. Pal, Emergent strong zero mode through local Floquet engineering, *Phys. Rev. B* **109**, 064303 (2024).
- [53] F. D. M. Haldane, Nonlinear field theory of large-spin Heisenberg antiferromagnets: Semiclassically quantized solitons of the one-dimensional easy-axis Néel state, *Phys. Rev. Lett.* **50**, 1153 (1983).
- [54] K. Hida, Crossover between the Haldane-gap phase and the dimer phase in the spin-1/2 alternating Heisenberg chain, *Phys. Rev. B* **45**, 2207 (1992).
- [55] M. Kohmoto and H. Tasaki, Hidden $Z_2 \times Z_2$ symmetry breaking and the Haldane phase in the $s = 1/2$ quantum spin chain with bond alternation, *Phys. Rev. B* **46**, 3486 (1992).
- [56] Ph. Jacquod, P. G. Silvestrov, and C. W. J. Beenakker, Golden rule decay versus Lyapunov decay of the quantum Loschmidt echo, *Phys. Rev. E* **64**, 055203(R) (2001).
- [57] F. Haake, M. Kuś, and R. Scharf, Classical and quantum chaos for a kicked top, *Z. Phys. B* **65**, 381 (1987).
- [58] S. Sinha, S. Ray, and S. Sinha, Fingerprint of chaos and quantum scars in kicked Dicke model: An out-of-time-order correlator study, *J. Phys.: Condens. Matter* **33**, 174005 (2021).
- [59] G. Vidal, Efficient classical simulation of slightly entangled quantum computations, *Phys. Rev. Lett.* **91**, 147902 (2003).
- [60] We also note that similar observations, albeit for a different model and observables, have been reported recently in Ref. [61].
- [61] D. Yuan, S.-Y. Zhang, Y. Wang, L.-M. Duan, and D.-L. Deng, Quantum information scrambling in quantum many-body scarred systems, *Phys. Rev. Res.* **4**, 023095 (2022).
- [62] D. Abanin, W. De Roeck, W. W. Ho, and F. Huveneers, A rigorous theory of many-body prethermalization for periodically driven and closed quantum systems, *Commun. Math. Phys.* **354**, 809 (2017).
- [63] X. Wen, R. Fan, and A. Vishwanath, Floquet's refrigerator: Conformal cooling in driven quantum critical systems, [arXiv:2211.00040](https://arxiv.org/abs/2211.00040).
- [64] G.-X. Su, H. Sun, A. Hudomal, J.-Y. Desaulles, Z.-Y. Zhou, B. Yang, J. C. Halimeh, Z.-S. Yuan, Z. Papić, and J.-W. Pan, Observation of unconventional many-body scarring in a quantum simulator, *Phys. Rev. Res.* **5**, 023010 (2023).
- [65] W. L. Tan, P. Becker, F. Liu, G. Pagano, K. S. Collins, A. De, L. Feng, H. B. Kaplan, A. Kyprianidis, R. Lundgren, W. Morong, S. Whitsitt, A. V. Gorshkov, and C. Monroe, Domain-wall confinement and dynamics in a quantum simulator, *Nat. Phys.* **17**, 742 (2021).

- [66] P. N. Jepsen, Y. K. “Eunice” Lee, H. Lin, I. Dimitrova, Y. Margalit, W. W. Ho, and W. Ketterle, Long-lived phantom helix states in Heisenberg quantum magnets, *Nat. Phys.* **18**, 899 (2022).
- [67] M. Fishman, S. R. White, and E. M. Stoudenmire, The ITensor software library for tensor network calculations, *SciPost Phys. Codebases* **4** (2022).
- [68] A. Sen, D. Sen, and K. Sengupta, Analytic approaches to periodically driven closed quantum systems: Methods and applications, *J. Phys.: Condens. Matter* **33**, 443003 (2021).
- [69] S. Vajna, K. Klobas, T. Prosen, and A. Polkovnikov, Replica resummation of the Baker-Campbell-Hausdorff series, *Phys. Rev. Lett.* **120**, 200607 (2018).
- [70] M. Bukov, L. D’Alessio, and A. Polkovnikov, Universal high-frequency behavior of periodically driven systems: From dynamical stabilization to Floquet engineering, *Adv. Phys.* **64**, 139 (2015).
- [71] L. D’Alessio and A. Polkovnikov, Many-body energy localization transition in periodically driven systems, *Ann. Phys.* **333**, 19 (2013).